



Integrated metal–organic framework and pressure/vacuum swing adsorption process design: Descriptor optimization

Xiang Zhang¹ | Teng Zhou^{1,2}  | Kai Sundmacher^{1,2} 

¹Process Systems Engineering, Max Planck Institute for Dynamics of Complex Technical Systems, Magdeburg, Germany

²Process Systems Engineering, Otto-von-Guericke University Magdeburg, Magdeburg, Germany

Correspondence

Teng Zhou, Process Systems Engineering, Max Planck Institute for Dynamics of Complex Technical Systems, Sandtorstr. 1, D-39106 Magdeburg, Germany.
Email: zhout@mpi-magdeburg.mpg.de

Funding information

Max-Planck-Gesellschaft (Ernst Dieter Gilles Postdoctoral Fellowship and OvGU Junior Professorship)

Abstract

An integrated metal–organic framework (MOF) and pressure/vacuum swing adsorption (P/VSA) process design framework is presented for gas separation. It consists of two steps: adsorbent descriptor optimization, and MOF matching. In the first step, MOFs are represented as a large set of chemical and geometric descriptors from which the most influential ones are selected via a multistep screening method and treated as design variables. The valid design space of the selected descriptors is confined using a tailored classifier model and logic constraints. Based on collected adsorption isotherms of 471 different MOFs, data-driven isotherm models are developed. Combining the design space, isotherms, and four-step P/VSA process models, an integrated MOF and P/VSA process design problem is formulated. MOF descriptors and process operating conditions are optimized to maximize the process performance. The obtained optimal descriptors and isotherms can be used to guide the discovery of high-performance MOFs in a subsequent MOF matching step. This article addresses the first descriptor optimization step exemplified by propene/propane separation.

KEYWORDS

data-driven models, integrated MOF and process design, MOF descriptors, multiscale modeling, pressure/vacuum swing adsorption, propene/propane separation

1 | INTRODUCTION

Pressure/vacuum swing adsorption (P/VSA) is a widely used technology for gas separation. It exploits different affinities of gases on solid adsorbents at different pressures to achieve the separation. Currently, multiple types of porous materials are used as adsorbents, such as metal–organic framework (MOF), zeolite, and activated carbon. Among these, MOFs are formed via the self-assembly of various molecular building blocks (i.e., metal nodes and organic linkers) in different topologies. The large variety of building blocks provide a near-infinite design space for MOFs.¹ Additionally, MOFs possess many superior properties such as ultrahigh porosity, controllable pore geometry, and a functional

pore surface. Thus, MOFs have great potential to achieve remarkable progress in adsorption-based gas separation.²

MOF-based gas separation can be achieved via four alternative mechanisms: equilibrium separation, kinetic separation, molecular sieving, and gate-opening separation. Equilibrium separation, based on a difference in species equilibrium gas loadings, is the most common method.³ To date, numerous MOFs with distinct isotherm characteristics have been experimentally synthesized by tailoring the MOF chemistry and structure (e.g., pore geometry and topology). Clearly, this trial-and-error experimental approach is time consuming and inefficient. Importantly, many MOFs created in the laboratory cannot lead to good process performance.⁴ As depicted in Figure 1, the design of an MOF for use in P/VSA processes is a multiscale design problem

This is an open access article under the terms of the Creative Commons Attribution License, which permits use, distribution and reproduction in any medium, provided the original work is properly cited.

© 2021 The Authors. *AIChE Journal* published by Wiley Periodicals LLC on behalf of American Institute of Chemical Engineers.

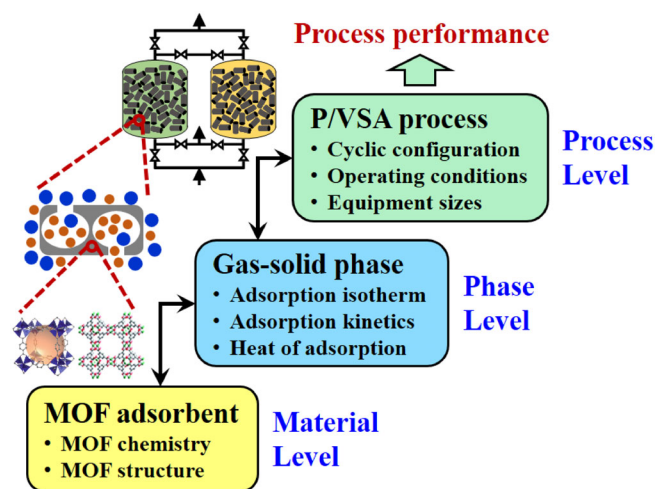


FIGURE 1 Multiscale structure of the pressure/vacuum swing adsorption process

that incorporates the inter-linked material, phase, and process levels. Variations of both material and process operating parameters affect the adsorption behavior of the gas–solid system and thus jointly determine the process performance. Bearing this multiscale picture in mind, a computational approach is highly desirable to expedite the identification of promising MOF adsorbents that can best serve the P/VSA process.^{5,6}

In the literature, computational screening methods have been employed to find suitable adsorbents, including MOFs and zeolites. The most popular one is high-throughput screening.^{7–12} A large set of synthesized or hypothetical adsorbents are first collected and their adsorption and diffusion properties are computed using molecular simulation. Then, various performance metrics (e.g., working capacity and selectivity) are calculated to identify top-ranked candidates for further process evaluation when applicable. Although this approach works for a large adsorbent database, those widely used metrics can neither tell whether separation requirements are satisfied nor rank the adsorbents correctly in terms of real process performance.^{13–15} Alternatively, hypothetical adsorption isotherms can be sampled and used for process optimization. With these results, surrogate models, which correlate isotherm characteristics with process performance, can be constructed and used for adsorbent screening.^{14,16–18} This method can generate an adsorbent ranking that is more consistent with process performance. However, like other screening approaches, it works only for adsorbents with known chemistry and structure. Besides, the insights from the phase and process levels cannot be used to guide new adsorbent design.

In addition to screening, the multiscale adsorbent and process design problem can be formulated as an optimization problem. Each level is represented by different models so that design variables at material and process levels can be simultaneously optimized. Such a strategy has been widely applied for integrated solvent and process design.^{19–23} Its success lies in the foundation of the computer-aided molecular design method, various molecular structure–property

relationship models, structural feasibility rules, and so on. For adsorption processes, by integrating the phase and process levels, Khurana and Farooq^{24,25} simultaneously optimized isotherm characteristics and VSA operating conditions for carbon capture. Optimal isotherm shapes achieving the highest process performance are obtained, which serve as targets for adsorbent design. However, without considering the valid design space of adsorbent materials, the isotherm targets may not correspond to any feasible adsorbents. Importantly, it is unknown which adsorbent chemistry and structure are favorable for the process. To tackle these issues, material design should be integrated directly into the process optimization framework. Unfortunately, no work has been done on this topic yet. The major challenge lies in the lack of explicit mathematical models to ensure the structural feasibility of the adsorbents and to predict the adsorbent properties (e.g., adsorption isotherm) based on their structures. For the instance of MOFs, hypothetical MOF materials are usually assembled using computational tools (e.g., ToBaCCo) and their structural feasibility is verified via *ab initio* calculations.²⁶ In addition, as stated above, computationally expensive molecular simulation is typically used to determine the adsorbent properties.²⁷ Clearly, it is difficult to incorporate these computations into a mathematical optimization problem.

In this article, focusing on the equilibrium separation, a novel integrated MOF and P/VSA process design framework is proposed in Figure 2 to tackle the above challenges. It consists of two steps: descriptor optimization, and MOF matching. Because of the vast number of MOF building blocks, it is hard to build mathematical models to predict adsorption isotherms directly from building blocks. Thus, in the first step, an MOF is denoted by a set of descriptors. Several data science techniques are adopted to select proper descriptors, define a valid design space, and build data-driven models for predicting the adsorption isotherms. This enables an explicit formulation of the integrated design problem where MOF descriptors and process operating conditions are simultaneously optimized to maximize the process performance. The optimal results are then used to guide the discovery of high-performance MOFs in the second step. This work addresses the first step, while the second step will be elaborated in a subsequent article. The entire framework is demonstrated on the separation of propene (PE) and propane (PA), which is currently achieved with energy-intensive cryogenic distillation. An optimal design of the MOF and P/VSA process is of great significance for energy-saving. The rest of the article is organized as follows: First, the specific workflow of the descriptor optimization step is introduced in detail. Afterward, the resulting optimization problem is solved for the PE/PA separation.

2 | WORKFLOW OF DESCRIPTOR OPTIMIZATION

Figure 3 illustrates the workflow of the descriptor optimization step. First, MOFs are represented by a large set of descriptors. With the collected single-component adsorption isotherm data, a much smaller subset of representative MOF descriptors is selected to serve as design variables. Meanwhile, these selected descriptors are used to

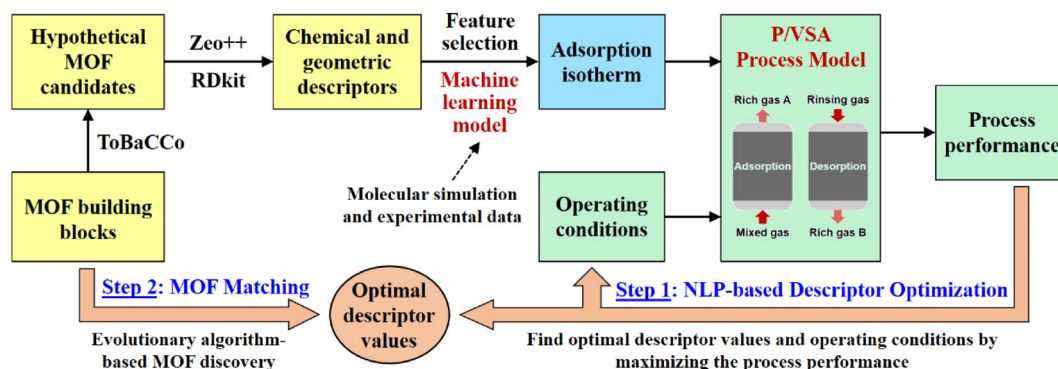


FIGURE 2 General methodology for integrated metal-organic framework and pressure/vacuum swing adsorption process design

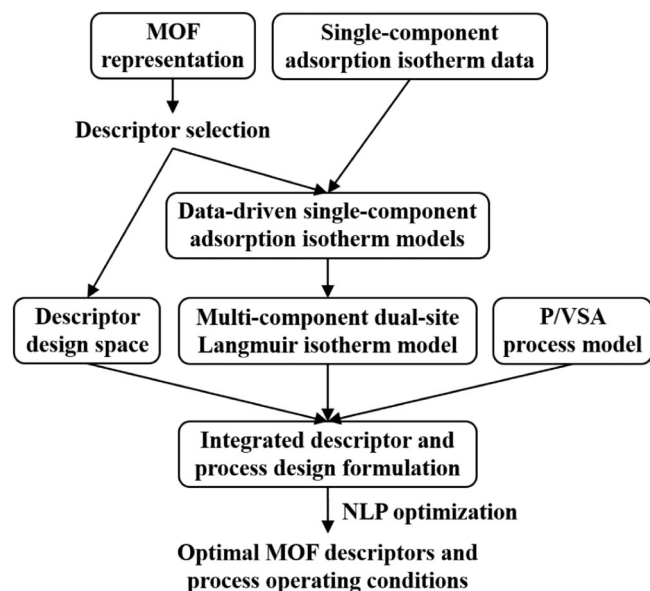


FIGURE 3 Workflow of the descriptor optimization step

develop data-driven models for predicting the single-component equilibrium adsorption loadings. Then, the data-driven models are employed to derive multicomponent dual-site Langmuir (DSL) isotherm models. In addition, based on the generated descriptor dataset, specific models are developed to define the valid design space of descriptors. Afterwards, by integrating the design space model, the DSL isotherm model, and the P/VSA process model, the integrated MOF and P/VSA process design task is formulated as a nonlinear programming (NLP) optimization problem. This problem is solved to identify the optimal descriptor values and process operating conditions. The detailed procedures and models are elaborated next.

2.1 | MOF representation

As a porous material, every MOF has a unique chemical composition (metal node and organic linker) and/or structure (pore geometry and topology). For adsorption, MOF chemistry greatly influences the

interaction with the adsorbate. For instance, some metals (e.g., copper and zinc) can form open metal site (OMS) that leads to a stronger interaction with olefins than with paraffins.^{28,29} In addition, since adsorbates tend to occupy the void spaces of an MOF during adsorption, pore geometry plays a crucial role in determining the adsorption capacity. Therefore, chemical and geometric descriptors are required to account for the effects of MOF chemistry and pore geometry on the adsorption properties.³⁰ For differentiating MOF topologies, topological descriptors can be computed. However, these descriptors are hard to interpret and trace back to specific topology.³¹ Additionally, only a small number of frequently used topologies can be found from the synthesized MOFs.^{1,32} Considering the low interpretability and limited topology variations, topological descriptors are thus not included as design variables here.

In this work, 14 widely used geometric descriptors are considered, including void fraction, volumetric surface area, largest cavity diameter, and unit cell size. It has been found that these descriptors can capture the important geometric characteristics of crystalline porous materials such as MOFs.³³ Moreover, Gharagheizi et al.³⁴ recently defined 5009 chemical descriptors to describe MOF chemistry. The definitions of these chemical descriptors are adjusted from molecular descriptors that have been widely used in cheminformatics. The current study employs these 5009 chemical descriptors directly. For easy reading, the symbols and definitions of all the 5023 descriptors are given in Appendix S1.

After specifying MOF descriptors, a set of real MOFs need to be selected and their corresponding descriptors can be calculated. The obtained descriptor data can then be used to develop data-driven models for predicting MOF adsorption isotherms. Here, 471 different MOFs are selected from the CoRE MOF database where stable and synthesizable MOFs with available atomic coordinates are collected.³⁵ These 471 MOFs include considerable diversity of chemistry, geometry, and topology. For each MOF, the 14 geometric descriptors are computed using the open-source package Zeo++ with a probe radius of 1.86 Å.^{33,36} Additionally, the molecular graph of MOFs containing atom positions and connections is read using the cheminformatics package RDkit,³⁷ and 5009 chemical descriptors are derived accordingly. As a demonstration, the calculated 5023 descriptors of the 471 MOFs are listed in Appendix S1.³⁴

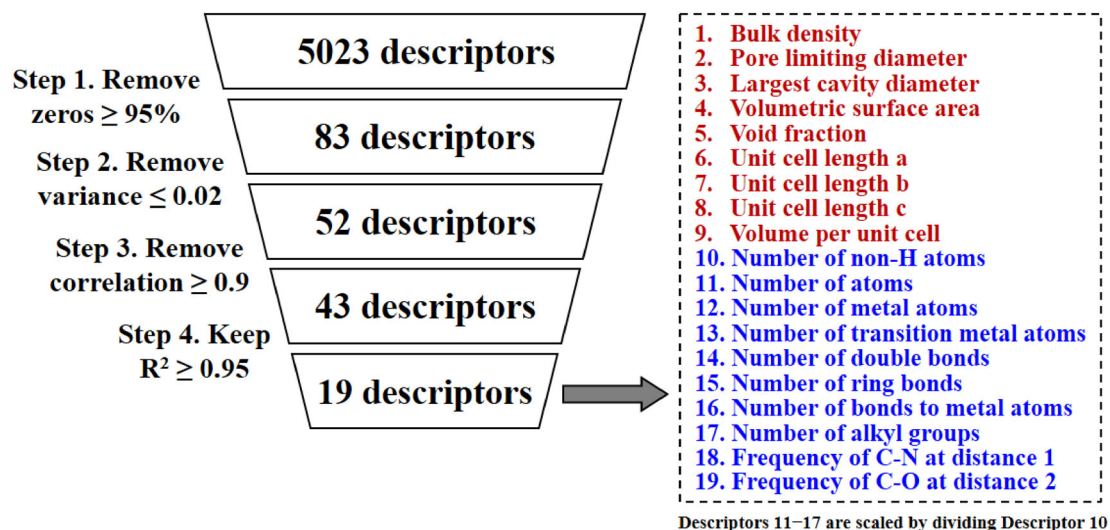


FIGURE 4 Detailed procedure for metal-organic framework descriptor selection

2.2 | Data-driven model for single-component adsorption isotherm

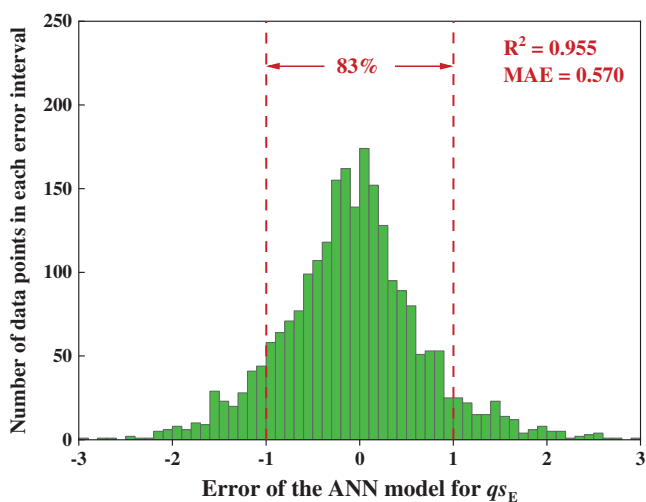
Data-driven models are developed to predict single-component equilibrium adsorption loadings using MOF descriptors as input. Clearly, a series of experimental or simulated adsorption isotherm data are required for model regression. The pure-species adsorption isotherms of PE and PA on the aforementioned 471 MOFs have been predicted by Tang et al.³⁸ using grand canonical Monte Carlo (GCMC) simulations at 300 K over the pressure range 0.1–156 bar. For easy reference, all the isotherm data are tabulated along with the MOF descriptors in Appendix S1.

Notably, although it is somehow useful to include a large number of descriptors, this brings difficulties in developing data-driven models and solving the descriptor optimization problem. Obviously, the effect of each descriptor on deciding the adsorption selectivity and capacity varies. For this reason, the most influential descriptors can be selected to build simple but reliable data-driven models.³⁹ Figure 4 shows a systematic procedure for descriptor selection.

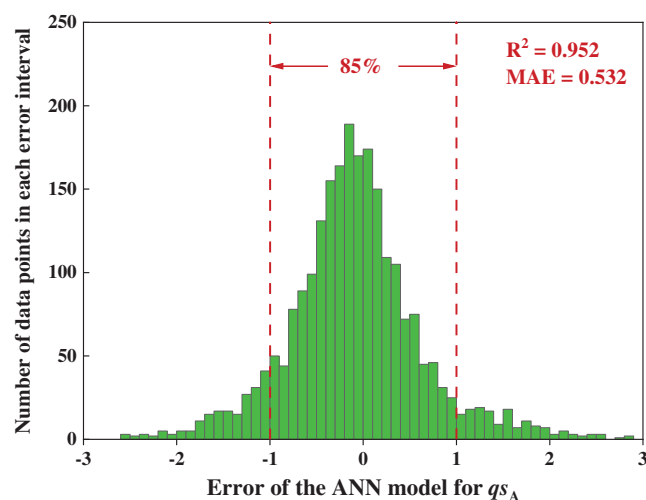
- In Step 1, the descriptors whose values are equal to zero for more than 95% of the 471 MOFs are removed. After this operation, a combination of 83 descriptors remains.
- In Step 2, the remaining descriptors are normalized into the range [0, 1]. Those descriptors whose variances are less than 0.02 are removed. This is because a descriptor usually has little predictive capability when it does not vary much. Fifty-two descriptors remain.
- When two descriptors are highly correlated, only one is worth retaining. In Step 3, if the correlation coefficient between any two descriptors exceeds 0.9, the descriptor having a larger total correlation coefficient with other descriptors is eliminated. After this step, 43 descriptors are left.
- In Step 4, the recursive feature elimination approach is applied to further reduce the number of descriptors.⁴⁰ Considering the

43 descriptors as input and equilibrium adsorption loadings as output, the sensitivity or importance of each descriptor is first computed using the random forest algorithm. Note that for different gas adsorbates, the descriptor sensitivities can be different. For instance, based on the PE adsorption loadings at 0.16 bar, the importance of the 43 descriptors is calculated and listed in Table S1. For predicting the PA adsorption loading at 0.10 bar, a different ranking of the descriptor importance is obtained (Table S1). After determining the relative importance of the descriptors, the least important descriptors are recursively removed and the remaining ones are sent to train artificial neural network (ANN) models to predict the isotherm data. For each trial, fivefold cross-validation is performed to tune the hyperparameters (number of layers and neurons). Figure S1 shows the evolutions of coefficient of determination (R^2), mean absolute error (MAE), and relative absolute error (RAE) of the ANN models for the prediction of PE and PA isotherm data. As expected, for both cases the model accuracy decreases when reducing the number of descriptors. To ensure R^2 larger than 0.95, two sets of the top-ranked 16 descriptors in Table S1 are selected for PE and PA, respectively. Within these two sets, 13 descriptors are repeated. Thus, in total 19 different descriptors (marked in blue in Table S1) are finally identified. As shown in Figure 4, they consist of 9 geometric and 10 chemical descriptors.

Based on the 19 descriptors, two new ANN models are trained for predicting the single-component equilibrium loadings of propene (q_{S_E}) and propane (q_{S_A}) at 300 K and different pressures, respectively. Again, fivefold cross-validation is carried out to find the optimal hyperparameters. As a result, each model has one input, one hidden, and one output layer while the *tansig* and *purelin* activation functions are applied in the hidden and output layers, respectively. The number of neurons in the hidden layer is 25 for the q_{S_E} model and 30 for the q_{S_A} model. The detailed model parameters are provided in



(A)



(B)

FIGURE 5 Prediction error distribution of the data-driven models for (A) q_{s_E} and (B) q_{s_A} at 300 K for 471 real metal–organic frameworks

Appendix S1, and the two data-driven models are summarized as follows:

$$q_{s_E} = \text{ANN}_1(y_1, \dots, y_{19}, P) \text{ at } T = 300 \text{ K}, \quad (1)$$

$$q_{s_A} = \text{ANN}_2(y_1, \dots, y_{19}, P) \text{ at } T = 300 \text{ K}, \quad (2)$$

where $y_1 - y_{19}$ are the 19 descriptor values, and P denotes the pressure. Figure 5 presents the histogram of prediction errors of these two models. For both models, over 80% of the deviations fall into the $[-1, 1]$ interval. For better assessment, R^2 and MAE are determined and given in Figure 5. As shown, the R^2 and MAE of both models are >0.95 and <0.6 , respectively. This indicates that the two models can generally provide reliable predictions on the single-component adsorption isotherms of propene and propane.

2.3 | Multicomponent dual-site Langmuir isotherm model

Adsorption-based gas separation occurs in a multicomponent environment. To predict the multicomponent adsorption equilibria, the DSL model is applied using pure-component model parameters (i.e., saturation capacity and adsorbent affinity) that are fitted from single-component adsorption loading data. It has been found that this type of DSL model can provide good predictions for many systems including PE/PA.⁴¹

In this work, the DSL model parameters are derived as follows: Given four pressures $P_i = \{0.01, 0.1, 1, 10\}$ bar, the corresponding single-component PE and PA adsorption loadings are predicted by

$$q_{s_{E,i}} = \text{ANN}_1(y_1, \dots, y_{19}, P_i) \text{ at } T = 300 \text{ K}. \quad (3)$$

$$q_{s_{A,i}} = \text{ANN}_2(y_1, \dots, y_{19}, P_i) \text{ at } T = 300 \text{ K}. \quad (4)$$

Meanwhile, the equilibrium adsorption loadings of PE and PA ($q_{E,i}^{eq}$ and $q_{A,i}^{eq}$) at pressure P_i can be calculated from the multi-component DSL model by assuming that only one component exists:

$$q_{E,i}^{eq} = \frac{Q_E^1 \cdot b_E^1 \cdot P_i \cdot y_E}{1 + b_E^1 \cdot P_i \cdot y_E + b_A^1 \cdot P_i \cdot y_A} + \frac{Q_E^2 \cdot b_E^2 \cdot P_i \cdot y_E}{1 + b_E^2 \cdot P_i \cdot y_E + b_A^2 \cdot P_i \cdot y_A} \quad y_E = 1, y_A = 0, \quad (5)$$

$$q_{A,i}^{eq} = \frac{Q_A^1 \cdot b_A^1 \cdot P_i \cdot y_A}{1 + b_E^1 \cdot P_i \cdot y_E + b_A^1 \cdot P_i \cdot y_A} + \frac{Q_A^2 \cdot b_A^2 \cdot P_i \cdot y_A}{1 + b_E^2 \cdot P_i \cdot y_E + b_A^2 \cdot P_i \cdot y_A} \quad y_E = 0, y_A = 1, \quad (6)$$

where y_E and y_A are the molar fractions of PE and PA in the gas phase, respectively. Equations (7) and (8) ensure that the adsorption loadings calculated from the two models match each other. With these, the eight DSL model parameters ($Q_E^1, b_E^1, Q_E^2, b_E^2, Q_A^1, b_A^1, Q_A^2,$ and b_A^2) can be obtained.

$$(q_{E,i}^{eq} - q_{s_{E,i}})^2 \leq 0.005. \quad (7)$$

$$(q_{A,i}^{eq} - q_{s_{A,i}})^2 \leq 0.005. \quad (8)$$

2.4 | Descriptor design space

Nineteen MOF descriptors are selected and two ANN models are developed from pure adsorption data without incorporating any thermodynamic basis. In this case, additional constraints should be added to confine the design solutions inside the valid design space of the models. In general, data-driven models are valid within the region that is densely covered by the training data, namely the validity domain.⁴² Consequently, any predictions outside the validity domain should be prevented. Usually, the convex hull of training data is approximated as the validity domain. However, the construction of such a convex hull is

computationally demanding for high-dimensional dataset, such as the 19-dimensional one in this work. An alternative approach is to build a one-class classifier. A suitable kernel function is used to map the original dataset into a new feature space where the boundary of the data points can be easily identified. Any points inside this boundary are considered as valid.⁴³ In this work, a one-class support vector machine (SVM) classifier is built to quantify the validity domain, where the radial basis function is selected as the kernel function. After importing the descriptor dataset, the kernel coefficient β is manually tuned to 2×10^{-9} to ensure that more than 99.5% of the training data are located inside the validity domain. The resulting classifier or boundary is written as

$$f(\mathbf{y}) = \sum_{j=1}^N w_j \cdot \phi_j(\mathbf{y}) + \rho > 0 \quad \mathbf{y} = [y_1, \dots, y_{19}], \quad (9)$$

$$\phi_j(\mathbf{y}) = e^{-\beta \|\mathbf{y} - \mathbf{SV}_j\|^2} \quad \mathbf{SV}_j = [SV_{1j}, \dots, SV_{19j}] \quad (10)$$

where N is the total number of fitted support vectors, ρ is the model intercept, and w_j is the coefficient of the j th support vector \mathbf{SV}_j . All these parameters were automatically fitted and are given in Appendix S1.

In order to generate valid design solutions, certain logic constraints have to be satisfied as well. Equation (11) ensures that each descriptor is within its lower and upper bounds, which are set as the minimal and maximal descriptor values in the training dataset:

$$\mathbf{y}^L \leq \mathbf{y} \leq \mathbf{y}^U \quad \mathbf{y} = [y_1, \dots, y_{19}]. \quad (11)$$

In addition, the largest cavity diameter (y_3) should be larger than the pore limiting diameter (y_2) based on their definitions.³³ The volume of a single unit cell (y_9) must be smaller than the cubic cell volume (i.e., $y_6 \cdot y_7 \cdot y_8$). Besides, the number of atoms (y_{10}) should be larger than the number of non-hydrogen atoms (y_{11}), and the number of metal atoms (y_{12}) must be larger than the number of transition-metal atoms (y_{13}). Finally, since the valency of one metal atom is typically less than 6, the total number of bonds linked to metal atoms (y_{16}) cannot exceed 6 times the number of metal atoms:

$$y_3 \geq y_2. \quad (12)$$

$$y_9 \leq y_6 \cdot y_7 \cdot y_8. \quad (13)$$

$$y_{10} \geq y_{11}. \quad (14)$$

$$y_{12} \geq y_{13}. \quad (15)$$

$$6y_{12} \geq y_{16}. \quad (16)$$

2.5 | P/VSA process model

Figure 6 depicts a one-bed, four-step P/VSA process for PE/PA separation. A complete process cycle consists of pressurization,

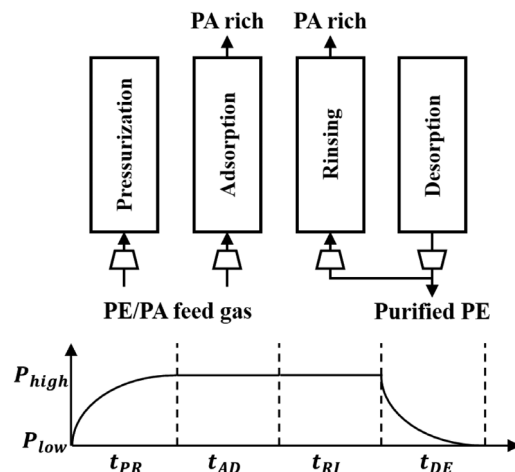


FIGURE 6 Schematic diagram of the four-step pressure/vacuum swing adsorption process

adsorption, rinsing, and desorption.⁴⁴ For pressurization, the feed gas is compressed to a high pressure (if necessary) and fed into the bottom of the column. The top is closed so that the internal pressure gradually increases. At the adsorption stage, the supply of feed gas is continued, where PE is selectively adsorbed and a PA-rich stream leaves from the top. Then, a small portion of the purified PE stream is re-pressurized and fed to the column to rinse the PA-rich gas in the void space. Note that at the rinsing step, the input gas compositions are presumably constant and equal to the average compositions of the purified PE stream. Afterward, a constant low pressure is enforced at the bottom of the column and the bed undergoes a desorption step where the pressure within the column is gradually reduced to a lower level and the released PE is collected at the bottom. In the end, the PE output is terminated and a new cycle can start. Note that the pressure history diagram in Figure 6 is used only for illustration and no specific pressure history is enforced at any step. For simplification, the following assumptions are made^{45,46}:

- The process is constantly operated at 300 K.
- Adsorbent properties (e.g., particle size and porosity) are uniform throughout the column.
- Both PE and PA follow the ideal gas law, and the gas viscosity is assumed to be constant.
- Axial dispersion in the packed adsorbent bed is neglected. In the radial direction, there are no variations of pressure and gas concentrations in both gas and solid phases.
- Regarding kinetics, the adsorption rates are approximated by linear driving force models. Since only the equilibrium separation of PE/PA is studied, lumped mass-transfer coefficients are considered and prespecified.
- The axial pressure drop is calculated from the Ergun equation.

Based on these assumptions, the mathematical model for the four-step P/VSA process is given in Appendix S1. It includes the component mass balances, the total mass balance, the mass-transfer kinetics,

the pressure drop correlation, the cyclic steady-state conditions, and the boundary conditions (see Equation (A1)–(A11)). Note that energy balances are not considered since isothermal process operation is assumed. Six operating conditions are treated as design variables at the process level. They are the durations of the four steps (t_{PR} , t_{AD} , t_{RI} , and t_{DE}) and two operating pressures (P_{low} and P_{high}). Since the energy consumption is a critical factor for assessing the process performance, the objective function is defined to minimize the total energy consumption per ton of the purified PE product:

$$\min E = \frac{E_{PR} + E_{AD} + E_{RI} + E_{DE}}{F_E^{out}}, \quad (17)$$

where E_{PR} , E_{AD} , E_{RI} , and E_{DE} are the energy consumption for pressurization, adsorption, rinsing, and desorption, respectively. F_E^{out} is the weight of purified PE produced in one process cycle. The equations for calculating these variables are given in Equations (A13)–(A21).⁴⁷

Moreover, the purity and recovery of each gas can be calculated. Equation (18) shows that the purity of PE is equal to the average PE molar fraction (y_E^{out}) in the outlet stream of desorption. In addition, the recovery of PE is expressed by Equation (19). In Figure 6, the bottom and top of the column are defined as $z=0$ and $z=L$, respectively, where L denotes the column length. u is the interstitial velocity, P represents the total pressure, and y_E^{in} is the molar fraction of PE in the feed gas.

$$\xi_E = y_E^{out} = \frac{\int_0^{t_{DE}} (u \cdot P \cdot y_E)|_{z=0} dt}{\int_0^{t_{DE}} (u \cdot P)|_{z=0} dt}. \quad (18)$$

$$\theta_E = \frac{\int_0^{t_{DE}} (u \cdot P \cdot y_E)|_{z=0} dt - P_{high} y_E^{out} \int_0^{t_{RI}} u|_{z=0} dt}{P_{high} y_E^{in} \left(\int_0^{t_{PR}} u|_{z=0} dt + \int_0^{t_{AD}} u|_{z=0} dt \right)}. \quad (19)$$

With these, the purity and recovery of PA can be simply calculated based on the overall input–output mass balances.

2.6 | Integrated design formulation

As indicated in Step 1 of the design framework (Figure 2), the integrated MOF and P/VSA process design problem is formulated and solved as a nonlinear optimization problem. Nineteen MOF descriptors denoting the variations of MOF chemistry and structure as well as 6 process operating conditions are simultaneously optimized to minimize the energy consumption. One-class SVM model and logic constraints account for the valid design space of descriptors. Two ANN models are built to predict the single-component adsorption isotherm and then used to fit the parameters of the multicomponent DSL isotherm model. At the process level, given prespecified equipment sizes, the energy consumption as well as product purity and recovery are calculated from the P/VSA process models. The recovery and purity of PE should be constrained according to industrial requirements.

$$\min_{x,y} E = \frac{E_{PR} + E_{AD} + E_{RI} + E_{DE}}{F_E^{out}} \quad \text{Objective function.} \quad (20)$$

| | |
|--|------------------------------------|
| s.t. Equation (9)–(16) | Descriptor design space |
| Equations (3)–(8) | Multi-component DSL isotherm model |
| Equations (18) and (19), (A1)–(A21) | P/VSA process model |
| $\theta_E \geq \theta_E^L$, $\xi_E \geq \xi_E^L$ | Separation specifications |
| $\mathbf{x} = [t_{PR}, t_{AD}, t_{RI}, t_{DE}, P_{high}, P_{low}]$ | Process operating conditions |
| $\mathbf{y} = [y_1, \dots, y_{19}]$ | Representative MOF descriptors |

Note that the optimization problem stated above cannot be solved directly since it contains both partial differential equations (PDEs) and algebraic equations. Here, a complete spatial and temporal discretization of PDEs is carried out for performing equation-oriented P/VSA process optimization. The entire column is divided into 20 identical sections, and the finite volume method with the upwind difference scheme is applied for spatial discretization. In addition, the backward Euler's scheme is used for temporal discretization. The durations of the pressurization and rinsing steps are discretized into 10 identical time intervals, while those of the other two steps are divided into 20 identical time intervals. By doing so, optimizing the durations of the four steps (i.e., t_{PR} , t_{AD} , t_{RI} , and t_{DE}) is equivalent to the optimization of the corresponding time-interval duration (i.e., Δt_{PR} , Δt_{AD} , Δt_{RI} , and Δt_{DE}). After the discretization, the P/VSA process model can be described by a branch of algebraic equations that are directly coded in GAMS for NLP optimization. For an easy understanding, the details on how discretization is performed are elaborated in Appendix S1.

3 | SEPARATION OF PROPENE/PROPANE FROM CATALYTIC CRACKING

As an example, the separation of a PE/PA mixture produced from the fluid catalytic cracking unit of a refinery is studied. Referring to the industrial conditions, the feed gas mole fraction of PE is set to 85% and the feed gas is at a pressure level of 2 atm.⁴⁴ It is assumed that the feed gas has already been cooled to 300 K, since our isotherm models are fitted at 300 K. Moreover, as an important raw material for polypropylene production, the purity of PE must be higher than 99%, which is set as a target for the adsorptive separation. Additionally, it has been observed that PE recovery is usually less than 30% when 99% PE is produced using P/VSA processes with not more than five steps.⁴⁸ Thus, the minimal PE recovery is set to 30%. The P/VSA process is modeled on a pilot-plant basis. Table 1 lists the input parameters including gas and adsorbent properties, equipment specifications, as well as limitations of operating conditions. Note that the lumped mass-transfer coefficients k are calculated by $k = \frac{15D_0}{r_p^2} e^{-\frac{E_A}{RT}}$, assuming that adsorbent particles are spherical and micro-pore diffusion is the rate-controlling step. For a certain gas, every MOF can have a different pre-exponential factor D_0 and activation energy E_A .

TABLE 1 Input parameters for the pressure/vacuum swing adsorption-based PE/PA separation

| Gas properties | | | |
|---|--------------------|--|--------------------|
| Molecular weight of PE (g/mol) | 42.1 | Molecular weight of PA (g/mol) | 44.1 |
| Gas viscosity (kg/m/s) | 8×10^{-6} | Isentropic coefficient of gas | 1.15 |
| Adsorbent properties | | | |
| Adsorbent particle density (kg/m ³) | 703 | Adsorbent particle radius (m) | 5×10^{-3} |
| Mass-transfer coefficient for PA (1/s) | 0.83 | Mass-transfer coefficient for PE (1/s) | 0.61 |
| Equipment specifications | | | |
| Bed porosity | 0.43 | Vacuum pump efficiency | 0.75 |
| Bed length (m) | 2 | Compressor efficiency | 0.75 |
| Bed diameter (m) | 0.4 | | |
| Bounds of operating conditions | | | |
| Pressurization duration (s) | 1–50 | Adsorption duration (s) | 1–200 |
| Rinsing duration (s) | 1–100 | Desorption duration (s) | 1–600 |
| High pressure (bar) | 1–10 | Low pressure (bar) | 0.01–1 |

TABLE 2 Parameters of the dual-site Langmuir isotherm model for Cu-BTC and optimal h-MOF

| | Cu-BTC | h-MOF |
|---------|--------|-------|
| Q_E^1 | 4.202 | 4.765 |
| b_E^1 | 96.17 | 1.556 |
| Q_E^2 | 4.059 | 0.100 |
| b_E^2 | 96.17 | 1000 |
| Q_A^1 | 4.511 | 2.093 |
| b_A^1 | 15.083 | 0.100 |
| Q_A^2 | 3.504 | 1.093 |
| b_A^2 | 15.083 | 6.700 |

Here, the D_0 and E_A representing PE and PA adsorptions in Cu-BTC are considered for simplicity, whose values have been reported by Wehring et al.⁴⁹ In addition, the micro-pore radius r_p is assumed as 56 μm . With all the above conditions, the lumped mass-transfer coefficients of PA and PE are calculated as 0.83 and 0.61, respectively.

3.1 | Benchmark process using Cu-BTC

The copper-based Cu-BTC (i.e., FIQCEN in the 471 MOFs), namely $\text{Cu}_3(\text{BTC})_2$ (BTC: benzene-1,3,5-tricarboxylate), has been recognized as one of the suitable MOFs for PE/PA separation due to its large adsorption capacity for PE.⁵⁰ Here, a benchmark P/VSA process using Cu-BTC as the adsorbent is optimized and used for comparison. The multicomponent DSL model of Cu-BTC is fitted using the reported experimental pure-component isotherm data,⁵¹ and the resulting model parameters are listed in Table 2. For easy illustration, the single-component equilibrium isotherm curves are plotted in Figure 7A. For Cu-BTC, the six process operating conditions are optimized to minimize the energy consumption. Because of the significant

model complexity, the optimization problem is solved in GAMS 27.2 using the local NLP solver CONOPT4. Different initializations are offered to obtain high-quality solutions. The best local optimum found is given in the second column of Table 3. The high pressure for adsorption is 1 atm when the initial selectivity $S_{\text{PE/PA}}$ is equal to 6.6 calculated with the parameters in Table 2. The low pressure for desorption is optimized to 0.011 atm and the minimum energy consumption is 505 kWh electricity per ton of PE.

Figure S2 shows the axial profiles of PE gas composition in the Cu-BTC process. As indicated, for pressurization, the PE composition tends to be lower than the initial composition 0.85 since a sudden high pressure drives the unsaturated Cu-BTC to selectively adsorb PE. As the adsorption continues, the adsorbent gradually becomes saturated until the PE gas composition reaches 0.85. Then, as the purified PE is fed into the column, its composition gradually increases at the rinsing step. Finally, by reducing the pressure at the desorption step, the captured PE is released and its gas composition further increases to 0.99.

3.2 | Optimal MOF and process from integrated design

Under the same requirements on PE purity and recovery, the integrated design problem in Equation (20) is solved. Again, the solver CONOPT4 and different initial values are used. The problem contains 10,800 single variables, 11,404 equations, and 58,831 nonlinear matrix entries. It takes about 150 s to find the optimal solution, as listed in the third column of Table 3. For convenience, the optimal MOF refers to a hypothetical MOF (h-MOF). Clearly, the process operating conditions are different from those of the benchmark process, particularly the two pressures. The high pressure is 2 atm, which is exactly equal to the initial pressure of the feed gas. The desorption occurs at 1 atm. Under such pressures, no gas compression is needed

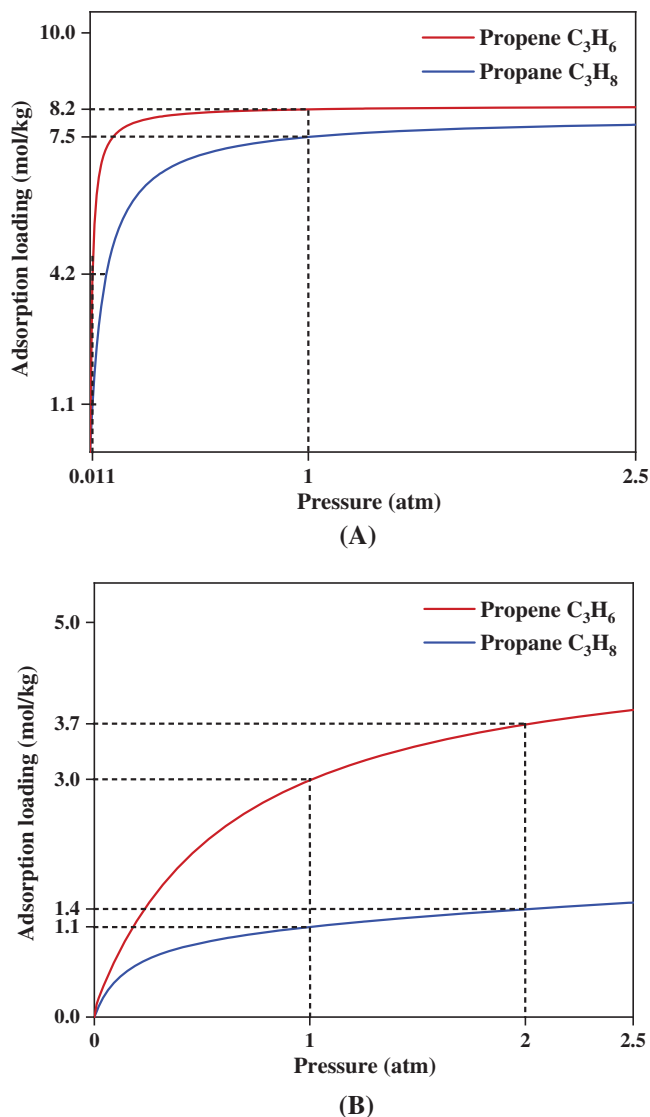


FIGURE 7 Adsorption isotherms at 300 K for (A) the benchmark Cu-BTC and (B) the optimal h-MOF

at the pressurization and adsorption steps and no evacuation is required for desorption. Only a small amount of electricity is consumed at the rinsing step to re-compress the low-pressure PE to the high pressure. The overall energy consumption is 12.8 kWh electricity per ton PE. Obviously, this is much lower than that of the benchmark process.

Figure S3 shows the axial profiles of PE compositions in a typical process cycle for the optimal h-MOF. Comparing with Figure S2, it can be found that the axial profiles in the two processes have similar shape and trend, in particular at the rinsing step. The major differences occur at the pressurization and desorption steps. For instance, because of the higher operating pressure, the releasing gas velocity is larger and thus the PE composition reaches 0.99 much faster in the h-MOF-based process. As indicated in Figures S2 and S3, the PE composition in the entire column at the beginning of pressurization is equivalent to that at the end of desorption, demonstrating the cyclic steady-state condition.

TABLE 3 Optimal operating conditions and performance of the Cu-BTC-based benchmark process and the h-MOF-based process

| | Benchmark process | Optimal process |
|---|-------------------|-----------------|
| PR duration (s) | 22.5 | 13.0 |
| AD duration (s) | 71.5 | 22.1 |
| RI duration (s) | 77.0 | 5.6 |
| DE duration (s) | 600 | 600 |
| High pressure (atm) | 1 | 2 |
| Low pressure (atm) | 0.011 | 1 |
| PE purity | 0.99 | 0.99 |
| PE recovery | 0.34 | 0.30 |
| PE production rate (mol/s) | 0.16 | 0.06 |
| Initial selectivity at high pressure | 6.6 | 33.9 |
| Energy consumption at pressurization (kWh/ton PE) | 0 | 0 |
| Energy consumption at adsorption (kWh/ton PE) | 1.2 | 0 |
| Energy consumption at rinsing (kWh/ton PE) | 184.3 | 12.8 |
| Energy consumption at desorption (kWh/ton PE) | 319.3 | 0 |
| Total energy consumption (kWh/ton PE) | 504.8 | 12.8 |

Abbreviation: PE, propene.

The large process variations are attributed to the significant differences of adsorption isotherms. As shown in Figure 7A, Cu-BTC has a poor PE desorption capability. A tough vacuum condition (i.e., 0.011 atm) is needed to meet the purity and recovery requirements. This directly leads to a large energy consumption at the rinsing and desorption stages (see Table 3). For the h-MOF in Figure 7B, the isotherms can provide a much better condition for adsorption and desorption. The PE loading difference between 1 and 2 atm reaches 0.7 mol/kg. Such a large gap at desirable pressures greatly facilitates PE desorption and recovery. In addition, Table 2 lists the fitted DSL model parameters for h-MOF. Note that three DSL model parameters of h-MOF reach the lower or upper limits, and the affinity parameters (e.g., b_E^1 and b_E^2) show a large energetic heterogeneity. Considering these, there is probably no real MOF that has exactly the same parameters or isotherms as h-MOF. However, the results can well reflect the characteristics that promising MOFs should possess. For PE, the saturation capacity at site 1 is much larger than that at site 2 (4.765 vs. 0.100). This suggests that for new MOFs, site 1 should play a dominant role on PE adsorption, regardless of the affinity difference. In addition, comparing the parameters of PE and PA at site 1, it is found that both the capacity and affinity of PE are larger than those of PA. Obviously, the new MOFs should provide a PE-selective site 1. For site 2, the capacity of PE is unfortunately smaller than that of PA (about 10 times difference) but not as significant as 47 times for site 1. In this case, the affinity of PE on site 2 should be as large as possible in order to compensate its relatively low capacity and try to compete against the

| Descriptor | Value | Descriptor | Value |
|--|-------|----------------------------------|-------|
| Bulk density (g/cm ³) | 1.9 | Number of atoms | 230 |
| Pore limiting diameter (Å) | 5.9 | Number of metal atoms | 46 |
| Largest cavity diameter (Å) | 7.0 | Number of transition metal atoms | 46 |
| Volumetric surface area (m ² /cm ³) | 279.4 | Number of double bonds | 14 |
| Void fraction | 0.82 | Number of ring bonds | 332 |
| Unit cell length <i>a</i> (Å) | 7.2 | Number of bonds to metal atoms | 18 |
| Unit cell length <i>b</i> (Å) | 11.0 | Number of alkyl groups | 5 |
| Unit cell length <i>c</i> (Å) | 7.5 | Frequency of C-N at distance 1 | 0.45 |
| Volume per unit cell (Å ³) | 589.1 | Frequency of C-O at distance 2 | 0 |
| Number of non-H atoms | 230 | | |

TABLE 4 Optimal metal-organic framework descriptors

adsorption of PA on site 2. Clearly, the result is a kind of compromise optimal solution under both material and process constraints.

With the parameters of h-MOF in Table 2, the initial selectivity at the adsorption condition (2 atm and 300 K) is calculated to be 33.9. This is much larger than that of Cu-BTC, mainly due to its much less PA adsorption capacity. Such a large selectivity helps achieving a high PE purity. On the other hand, because of the large PE adsorption capacity of Cu-BTC, the benchmark process has a higher PE production rate than our optimal process, although it needs a longer duration for one process cycle. Based on the above analysis, several adsorbent design guidelines can be extracted. First, a large selectivity and small PA adsorption capacity are beneficial for increasing the PE purity and recovery. Second, the PE adsorption capacity has a substantial effect on its production rate. This agrees well with previous findings.²⁴ Finally, to enable an energy-efficient separation, the adsorbent should offer a good adsorption-desorption balance that can better match the feed gas conditions.

Table 4 lists the optimal MOF descriptor values. Important information can be drawn and used for the subsequent MOF matching. For the pore geometry, a relatively small cavity diameter and volumetric surface area are preferred. It has been found that the former improves the selectivity of PE over PA, and the latter may result in a small adsorption capacity of PA, helping to increase the selectivity as well.^{2,10} For MOF chemistry, using transition metals is desirable. As is widely known, transition metals (e.g., copper and zinc) can introduce OMS and π -complexation, which lead to stronger interactions with PE than with PA.²⁹ Regarding the organic linker, it is better to use groups consisting of rings and double bonds as well as C-N bonds. Finally, it is not recommended to use organic linkers forming C-O pairs at topological distance 2 (i.e., with C-X-O chains), such as benzoic acid and furan.

4 | REMARK FOR MOF MATCHING

In this work, the optimal MOF descriptors and isotherms were identified within the confined design space. In the subsequent MOF matching step (see Figure 2), our aim is to find new, promising MOFs matching the optimal descriptors and isotherms. First, based on the

information drawn from the optimal descriptors, a set of MOF building blocks will be identified and utilized for the computer-aided synthesis of new hypothetical MOFs. Second, the descriptors of the synthesized MOFs will be calculated to predict the corresponding isotherms via the established ANN model. Afterward, based on the optimal isotherms, certain isotherm-process performance relationships will be explicitly studied to serve as a preliminary tool for fast screening of the MOFs. Then, the screened MOFs will be ranked according to the magnitude of the difference between their descriptors and the optimal ones. Finally, the process performance of the top candidates will be evaluated to identify the real optimal MOF.

5 | CONCLUSION

This paper presented a new two-step framework for integrated MOF and P/VSA process design. In the first step, MOFs were denoted as a set of selected descriptors serving as design variables. With these descriptors, data-driven models were developed to describe the valid descriptor design space and to predict the adsorption isotherms. Combining the design-space validity model, isotherm model, and P/VSA process model, the integrated design problem was explicitly formulated as an NLP problem where MOF descriptors and process operating conditions were simultaneously optimized to maximize the process performance. The proposed methodology was demonstrated on a PE/PA separation example. The results showed that the identified optimal process could significantly reduce the energy consumption compared to a benchmark process, using the Cu-BTC as the adsorbent. The obtained optimal descriptors and corresponding isotherm curves can serve as design targets for the discovery of new, promising MOFs in a subsequent matching step.

The largest novelty of the present work is the use of a multiscale modeling approach to integrate the variations of MOF chemistry and structure into P/VSA process design. This provides a reliable and efficient way for computational adsorbent design to maximize the practical adsorption process performance. Despite this large progress, the current work still has some limitations. For instance, because of the lack of relevant data, the impact of the heat of adsorption is neglected and thus isothermal processes are assumed. Note that the heat of adsorption can be estimated using GCMC simulations. Given a series

of training data, it is possible to develop another data-driven model to predict the heat of adsorption. Integrating this model will help describe the effect of the heat of adsorption on adsorption loadings and consequently on process performance. Moreover, a simple one-bed, four-step P/VSA process is considered. In future, more sophisticated adsorption processes with multiple beds and more steps can be applied to further enhance the product recovery. In that case, the development of surrogate models for substituting the complex P/VSA processes can be a viable option.⁵²

ACKNOWLEDGMENTS

Financial support from Max Planck Society, Germany, to the Ernst Dieter Gilles Postdoctoral Fellowship for Xiang Zhang and to the OvGU Junior Professorship of Teng Zhou on computer-aided material and process design (CAMPD) is gratefully acknowledged. Open Access funding enabled and organized by Projekt DEAL.

AUTHOR CONTRIBUTIONS

Xiang Zhang: Investigation (lead); writing – original draft (lead). **Teng Zhou:** Methodology (equal); supervision (lead); writing – review and editing (lead). **Kai Sundmacher:** Conceptualization (equal); resources (lead); writing – review and editing (equal).

DATA AVAILABILITY STATEMENT

The data that supports the findings of this study are available in the supplementary material of this article.

ORCID

Teng Zhou  <https://orcid.org/0000-0003-1941-5348>

Kai Sundmacher  <https://orcid.org/0000-0003-3251-0593>

REFERENCES

1. Yao Z, Sánchez-Lengeling B, Bobbitt NS, et al. Inverse design of nanoporous crystalline reticular materials with deep generative models. *Nat Mach Intell*. 2021;3(1):76–86.
2. Wang T, Lin E, Peng Y-L, Chen Y, Cheng P, Zhang Z. Rational design and synthesis of ultramicroporous metal-organic frameworks for gas separation. *Coord Chem Rev*. 2020;423:213485.
3. Bao Z, Chang G, Xing H, Krishna R, Ren Q, Chen B. Potential of microporous metal-organic frameworks for separation of hydrocarbon mixtures. *Energ Environ Sci*. 2016;9(12):3612–3641.
4. Burns TD, Pai KN, Subraveti SG, et al. Prediction of MOF performance in vacuum swing adsorption systems for postcombustion CO₂ capture based on integrated molecular simulations, process optimizations, and machine learning models. *Environ Sci Technol*. 2020;54(7):4536–4544.
5. Pullumbi P, Brandani F, Brandani S. Gas separation by adsorption: technological drivers and opportunities for improvement. *Curr Opin Chem Eng*. 2019;24:131–142.
6. Asgari M, Streb A, van der Spek M, Queen W, Mazzotti M. Synergistic material and process development: application of a metal-organic framework, Cu-TDPAT, in single-cycle hydrogen purification and CO₂ capture from synthesis gas. *Chem Eng J*. 2021;414:128778.
7. Daglar H, Keskin S. Recent advances, opportunities, and challenges in high-throughput computational screening of MOFs for gas separations. *Coord Chem Rev*. 2020;422:213470.
8. Wilmer CE, Leaf M, Lee CY, et al. Large-scale screening of hypothetical metal-organic frameworks. *Nat Chem*. 2012;4(2):83–89.
9. First EL, Hasan MMF, Floudas CA. Discovery of novel zeolites for natural gas purification through combined material screening and process optimization. *AIChE J*. 2014;60(5):1767–1785.
10. Yeo BC, Kim D, Kim H, Han SS. High-throughput screening to investigate the relationship between the selectivity and working capacity of porous materials for propylene/propane adsorptive separation. *J Phys Chem C*. 2016;120(42):24224–24230.
11. Li Z, Zhang Y, Liu B, Chen G, Smit B. Multilevel screening of computation-ready, experimental metal-organic frameworks for natural gas purification. *AIChE J*. 2021;67(7):e17279.
12. Yan Y, Zhang L, Li S, Liang H, Qiao Z. Adsorption behavior of metal-organic frameworks: from single simulation, high-throughput computational screening to machine learning. *Comput Mater Sci*. 2021;193:110383.
13. Rajagopalan AK, Avila AM, Rajendran A. Do adsorbent screening metrics predict process performance? A process optimisation based study for post-combustion capture of CO₂. *Int J Greenh Gas Control*. 2016;46:76–85.
14. Khurana M, Farooq S. Adsorbent screening for postcombustion CO₂ capture: a method relating equilibrium isotherm characteristics to an optimum vacuum swing adsorption process performance. *Ind Eng Chem Res*. 2016;55(8):2447–2460.
15. Ga S, Jang H, Lee JH. New performance indicators for adsorbent evaluation derived from a reduced order model of an idealized PSA process for CO₂ capture. *Comput Chem Eng*. 2017;102:188–212.
16. Arora A, Iyer SS, Hasan MMF. Computational material screening using artificial neural networks for adsorption gas separation. *J Phys Chem C*. 2020;124:21446–21460.
17. Pai KN, Prasad V, Rajendran A. Generalized, adsorbent-agnostic, artificial neural network framework for rapid simulation, optimization, and adsorbent screening of adsorption processes. *Ind Eng Chem Res*. 2020;59(38):16730–16740.
18. Sen T, Kawajiri Y, Realff MJ. Integration of material and process design for kinetic adsorption separation. *Ind Eng Chem Res*. 2021;60(6):2536–2546.
19. Adjiman CS, Sahinidis NV, Vlachos DG, Bakshi B, Maravelias CT, Georgakis C. Process systems engineering perspective on the design of materials and molecules. *Ind Eng Chem Res*. 2021;60:5194–5206.
20. Zhou T, McBride K, Zhang X, Qi Z, Sundmacher K. Integrated solvent and process design exemplified for a Diels–Alder reaction. *AIChE J*. 2015;61(1):147–158.
21. Burger J, Papaioannou V, Gopinath S, Jackson G, Galindo A, Adjiman CS. A hierarchical method to integrated solvent and process design of physical CO₂ absorption using the SAFT- γ Mie approach. *AIChE J*. 2015;61(10):3249–3269.
22. Stavrou M, Lampe M, Bardow A, Gross J. Continuous molecular targeting–computer-aided molecular design (CoMT–CAMD) for simultaneous process and solvent design for CO₂ capture. *Ind Eng Chem Res*. 2014;53(46):18029–18041.
23. Zhang L, Pang J, Zhuang Y, Liu L, Du J, Yuan Z. Integrated solvent-process design methodology based on COSMO-SAC and quantum mechanics for TMQ (2,2,4-trimethyl-1,2-H-dihydroquinoline) production. *Chem Eng Sci*. 2020;226:115894.
24. Khurana M, Farooq S. Integrated adsorbent-process optimization for carbon capture and concentration using vacuum swing adsorption cycles. *AIChE J*. 2017;63(7):2987–2995.
25. Khurana M, Farooq S. Integrated adsorbent process optimization for minimum cost of electricity including carbon capture by a VSA process. *AIChE J*. 2019;65(1):184–195.
26. Boyd PG, Lee Y, Smit B. Computational development of the nanoporous materials genome. *Nat Rev Mater*. 2017;2(8):17037.
27. Iyer SS, Hasan MMF. Mapping the material-property space for feasible process operation: application to combined natural-gas separation and storage. *Ind Eng Chem Res*. 2019;58(24):10455–10465.

28. Jorge M, Fischer M, Gomes JRB, Siquet C, Santos JC, Rodrigues AE. Accurate model for predicting adsorption of olefins and paraffins on MOFs with open metal sites. *Ind Eng Chem Res.* 2014;53(40):15475-15487.
29. Zhang Y, Li B, Krishna R, et al. Highly selective adsorption of ethylene over ethane in a MOF featuring the combination of open metal site and π -complexation. *Chem Commun.* 2015;51(13):2714-2717.
30. Chong S, Lee S, Kim B, Kim J. Applications of machine learning in metal-organic frameworks. *Coord Chem Rev.* 2020;423:213487.
31. Krishnapriyan AS, Montoya J, Haranczyk M, Hummelshøj J, Morozov D. Machine learning with persistent homology and chemical word embeddings improves prediction accuracy and interpretability in metal-organic frameworks. *Sci Rep.* 2021;11(1):8888.
32. Shevchenko AP, Alexandrov EV, Golov AA, Blatova OA, Duyunova AS, Blatov VA. Topology versus porosity: what can reticular chemistry tell us about free space in metal-organic frameworks? *Chem Commun.* 2020;56(67):9616-9619.
33. Willems TF, Rycroft CH, Kazi M, Meza JC, Haranczyk M. Algorithms and tools for high-throughput geometry-based analysis of crystalline porous materials. *Microporous Mesoporous Mater.* 2012;149(1):134-141.
34. Gharagheizi F, Tang D, Sholl DS. Selecting adsorbents to separate diverse near-azeotropic chemicals. *J Phys Chem C.* 2020;124(6):3664-3670.
35. Chung YG, Haldoupis E, Bucior BJ, et al. Advances, updates, and analytics for the computation-ready, experimental metal-organic framework database: CoRE MOF 2019. *J Chem Eng Data.* 2019;64(12):5985-5998.
36. Moosavi SM, Nandy A, Jablonka KM, et al. Understanding the diversity of the metal-organic framework ecosystem. *Nat Commun.* 2020; 11(1):4068.
37. RDKit: Open-source cheminformatics. Accessed May 2021. <http://www.rdkit.org>
38. Tang D, Wu Y, Verploegh RJ, Sholl DS. Efficiently exploring adsorption space to identify privileged adsorbents for chemical separations of a diverse set of molecules. *ChemSusChem.* 2018;11(9): 1567-1575.
39. Lee JH, Shin J, Realff MJ. Machine learning: overview of the recent progresses and implications for the process systems engineering field. *Comput Chem Eng.* 2018;114:111-121.
40. Jablonka KM, Ongari D, Moosavi SM, Smit B. Big-data science in porous materials: materials genomics and machine learning. *Chem Rev.* 2020;120(16):8066-8129.
41. Ritter JA, Bhadra SJ, Ebner AD. On the use of the dual-process Langmuir model for correlating unary equilibria and predicting mixed-gas adsorption equilibria. *Langmuir.* 2011;27(8):4700-4712.
42. Kahrs O, Marquardt W. The validity domain of hybrid models and its application in process optimization. *Chem Eng Process.* 2007;46(11): 1054-1066.
43. Schweidtmann AM, Weber JM, Wende C, Netze L, Mitsos A. Obey validity limits of data-driven models through topological data analysis and one-class classification. *Optim Eng.* 2021. <https://doi.org/10.1007/s11081-021-09608-0>
44. Khalighi M, Karimi IA, Farooq S. Comparing SiCHA and 4A zeolite for propylene/propane separation using a surrogate-based simulation/ optimization approach. *Ind Eng Chem Res.* 2014;53(44):16973-16983.
45. Park J-H, Kim J-N, Cho S-H. Performance analysis of four-bed H₂ PSA process using layered beds. *AIChE J.* 2000;46(4):790-802.
46. Agarwal A, Biegler LT, Zitney SE. Simulation and optimization of pressure swing adsorption systems using reduced-order modeling. *Ind Eng Chem Res.* 2009;48(5):2327-2343.
47. Leperi KT, Snurr RQ, You F. Optimization of two-stage pressure/vacuum swing adsorption with variable dehydration level for postcombustion carbon capture. *Ind Eng Chem Res.* 2016;55(12): 3338-3350.
48. Grande CA, Rodrigues AE. Propane/propylene separation by pressure swing adsorption using zeolite 4A. *Ind Eng Chem Res.* 2005;44(23): 8815-8829.
49. Wehring M, Gascon J, Dubbeldam D, Kapteijn F, Snurr RQ, Stallmach F. Self-diffusion studies in CuBTC by PFG NMR and MD simulations. *J Phys Chem C.* 2010;114(23):10527-10534.
50. Ferreira AFP, Santos JC, Plaza MG, Lamia N, Loureiro JM, Rodrigues AE. Suitability of Cu-BTC extrudates for propane-propylene separation by adsorption processes. *Chem Eng J.* 2011;167(1):1-12.
51. Lamia N, Jorge M, Granato MA, Almeida Paz FA, Chevreau H, Rodrigues AE. Adsorption of propane, propylene and isobutane on a metal-organic framework: molecular simulation and experiment. *Chem Eng Sci.* 2009;64(14):3246-3259.
52. Leperi KT, Yancy-Caballero D, Snurr RQ, You F. 110th anniversary: surrogate models based on artificial neural networks to simulate and optimize pressure swing adsorption cycles for CO₂ capture. *Ind Eng Chem Res.* 2019;58(39):18241-18252.

SUPPORTING INFORMATION

Additional supporting information may be found in the online version of the article at the publisher's website.

How to cite this article: Zhang X, Zhou T, Sundmacher K. Integrated metal-organic framework and pressure/vacuum swing adsorption process design: Descriptor optimization. *AIChE J.* 2022;68(2):e17524. doi:10.1002/aic.17524